Discover Civil Engineering

RESEARCH Open Access

Finite element analysis and empirical design models for the flexural capacity of reinforced concrete beams enclosing smooth and perforated cold formed sections

Mohamed Eldeib[1], Nader Khalil[1], Ashraf Abou-Rayan[1] and Ahmed Youssef Kamal[1*]

*Correspondence:
Ahmed Youssef Kamal
ahmed.mohamed@bhit.bu.edu.eg
[1]Civil Engineering Department, Benha Faculty of Engineering, Fareed Nada Street, Benha 13518, Qalyubia Governorate, Egypt

Abstract

This study investigates the flexural behavior of reinforced concrete beams encasing smooth and perforated cold-formed steel (CFS) sections. A comprehensive three-dimensional nonlinear finite element (FE) model was developed in ANSYS to simulate the load–deflection response and ultimate capacity of composite beams. Validation against experimental results showed that discrepancies in ultimate load and mid-span deflection were within ±7%. A parametric study assessed the influence of CFS thickness, height, and configurations (back-to-back, front-to-front, U, and n-shapes). Results revealed that increasing CFS thickness and height significantly enhanced stiffness and ultimate load. While perforations slightly reduced the ultimate capacity in some cases, they significantly improved ductility through enhanced mechanical interlock. Finally, high-order polynomial empirical design models (Z-K and Z-M equations) were proposed to predict the ultimate load enhancement ratio (Z) with high correlation ($R^2 > 0.97$). These formulas, validated for thickness ratios (K) up to 4% and height ratios (M) up to 0.9, provide a reliable and practical tool for the preliminary design and optimization of composite beams within these geometric limits.

Keywords Encased beams, Cold-formed steel Section, Perforated sections, Flexural strength

1 Introduction

Cold-formed steel (CFS) sections are increasingly used in modern structural systems owing to their favorable strength-to-weight ratio, ease of fabrication, and adaptability to prefabrication and modular construction. When combined with concrete by encasement, thin-walled CFS profiles form hybrid composite members that exploit the compressive stiffness and confinement of concrete and the tensile strength and ductility of steel, producing structural elements with enhanced flexural and shear performance under both monotonic and cyclic loading [1, 17, 24]. Experimental evidence

demonstrates that concrete casement effectively restrains local buckling of thin plates in CFS profiles and improves post-peak energy dissipation compared with bare CFS members [1, 22, 23]. Abou-Rayan et al. [1] studied RC beams containing either smooth (flat) or perforated CFS sections and reported notable gains in stiffness, ultimate moment and ductility; their work also highlighted the sensitivity of composite action to perforation geometry, section thickness and section position within the beam cross-section. Complementary studies have shown that filling CFS sections with tailored concrete mixes (including lightweight and recycled aggregate concretes) or using engineered cementitious composites (ECC) as infill can further enhance the bending capacity and ductility of composite members [2, 12].

Perforated CFS members are adopted in practice to reduce self-weight and to facilitate routing of services. However, perforations introduce local changes in stiffness and stress distribution and may promote web-crippling and local buckling phenomena that reduce capacity unless appropriately accounted for. Several recent experimental and numerical investigations have therefore examined perforation effects on web crippling and flexural behavior for uncased CFS channels and Z-sections [9, 6, 13, 21]. Elkassas et al., [7] and Lotfy et al., [10] further explored strengthening and encasement strategies for instance, ferrocement jackets or lightweight concrete encasement, demonstrating the interaction between perforation pattern and the encasement material in controlling local instability and bond behavior. Advanced numerical studies have produced efficient FE frameworks able to capture combined local/global buckling, plate-instability modes, and concrete–steel interface behavior in composite members [8, 11, 15]. Parametric FE studies exploring stiffeners, cross-section optimization and infill material effects have recently been reported, offering deeper insight into the influence of geometric tuning on ultimate capacity [5, 8, 14]. Nevertheless, most of the existing literature either investigates uncased perforated CFS elements, tests a limited set of thicknesses, or focuses on infill strategies without producing generalizable design equations. While previous studies, such as Yu et al., [24], focused primarily on solid composite sections, and Sheta et al., [17] investigated specialized materials like PE-ECC, there remains a significant gap regarding the mechanistic interaction between reinforced concrete and perforated CFS sections. Furthermore, very recent advancements in 2025 and 2026, such as those by Shen et al., [16] and Wang and Miller [19], have continued to explore the synergy between cold-formed sections and innovative infills. The influence of perforation geometry on the structural response of cold-formed steel has been further underlined by Vadivelu et al., [18], who identified that both the number and diameter of openings are critical factors influencing load-carrying capacity in rectangular hollow sections. Their findings demonstrated that while increasing the number of perforations typically reduces structural integrity, specific configurations such as circular openings with a diameter equal to 50% of the web depth can optimize bending performance. Similarly, Chandramohan et al., [4] demonstrated that edge-stiffened elongated web holes can enhance the moment capacity of CFS channels by 9% compared to unstiffened openings. Their findings indicated that current design standards are overly conservative, necessitating modified equations to accurately capture the flexural behavior of stiffened perforated sections. Furthermore, Chandramohan et al., [3] investigated the axial capacity of CFS channels with elongated edge-stiffened web holes, proposing modified design equations after identifying that stiffened openings significantly enhance structural stability

under compression. While such studies emphasize the benefits of mechanical stiffening for uncased sections, the interaction between these perforated profiles and concrete encasement under flexural loading remains a critical area for investigation. In contrast to these studies, the present work extends these research efforts by providing a specific quantification of the 'plugging effect' where concrete encased within perforations acts as a mechanical interlock, a phenomenon that remains poorly understood in existing literature. This study uniquely addresses this gap by extending the experimental foundation of Abou-Rayan et al. [1] and Youssef and Khalil [23] through a validated nonlinear 3-D finite element (FE) model. The model is used in a systematic parametric campaign to quantify the combined influence of perforation geometry, CFS thickness, and section height on load–deflection curves and local buckling modes. Based on the results, high-order empirical design equations (Z–K and Z–M) are proposed to enable practical prediction and optimization of composite beams, offering a direct design contribution that bridges the gap between theoretical modeling and current code limitations.

2 Methodology

2.1 Finite element modelling

A total of forty-nine three-dimensional nonlinear finite element (FE) models were developed using ANSYS to investigate the flexural performance of reinforced concrete (RC) beams encasing smooth and perforated cold-formed steel (CFS) sections. The models were loaded under mid-span vertical loads until failure to simulate the experimental setup conducted by Abou-Rayan et al. [1]. The FE models were validated against eleven experimental specimens, after which they were extended for a comprehensive parametric study. Parameters included the CFS section type (smooth or perforated), thickness, height, and arrangement. The primary outputs were ultimate load, mid-span deflection, and failure mode, which were used to assess the model's predictive accuracy and to perform parametric analysis.

2.2 Element types and material properties

The finite element modeling was performed in ANSYS, employing several element types to accurately represent the composite behavior of the encased beam system. The SOLID65 element was used to simulate the concrete material, capable of capturing both cracking and crushing phenomena. The SOLID186 twenty-node element modeled the bearing and loading plates, while the SOLID185 eight-node brick element represented the cold-formed steel (CFS) sections. Reinforcing bars and supports were modeled using the LINK180 element to simulate the axial behavior of steel reinforcement. Detailed geometric properties were incorporated into the model, including longitudinal reinforcement of two 12 mm diameter bars and 8 mm diameter stirrups at 150 mm intervals. The CFS perforations were modeled with a constant diameter and spacing to evaluate their mechanistic impact on the web's stability. To ensure the convergence and stability of the numerical results, a mesh sensitivity analysis was conducted prior to the parametric study. Various element sizes, ranging from 10 mm to 30 mm, were evaluated. It was observed that reducing the element size from 20 mm to 10 mm resulted in a marginal variation of less than 2% in the predicted ultimate flexural capacity, while significantly increasing the computational time. Consequently, a maximum element size of 20 mm was adopted for all subsequent models as it provided an optimal balance between

numerical accuracy and computational efficiency, as illustrated in Fig. 1. The interface between the cold-formed steel (CFS) section and the surrounding concrete was modeled using a perfect bond assumption. This approach is justified by the high degree of confinement provided by the encased configuration, which prevents significant slip between the components. Furthermore, the presence of perforations in the CFS web facilitates mechanical interlocking with the concrete matrix, effectively enhancing the bond strength and ensuring robust composite action. While this modeling strategy has been successfully validated in similar studies on encased composite members where interfacial slip was found to be negligible under flexural loading, it is important to acknowledge that this assumption may represent a limitation for configurations with exceptionally low concrete confinement or under extreme cyclic loading conditions where bond-slip effects could become more pronounced. To ensure geometric consistency and reproducibility, all perforation details including the specific hole dimensions, shapes, and longitudinal spacing were adopted directly from the experimental benchmark study by Abou-Rayan et al. [1]. These parameters were systematically integrated into the FE model to replicate the physical specimens where the stirrups traverse through the CFS web openings to act as shear connectors. By defining these variables, the study moves beyond a binary 'smooth vs. perforated' comparison, allowing for a detailed assessment of how the opening rate influences localized stress concentrations and the overall buckling behavior of the encased sections. Furthermore, the current fixed parameters were selected to maintain strict consistency with the physical experimental specimens used for validation, thereby providing a controlled baseline for quantifying the individual and combined effects of thickness and height ratios.

2.3 Material modeling and constitutive laws

The material modeling adopted experimentally validated constitutive laws to ensure accurate representation of the composite behavior. The concrete was modeled using a multilinear isotropic law, with a compressive strength (f_{cu}) of 31 MPa and a tensile

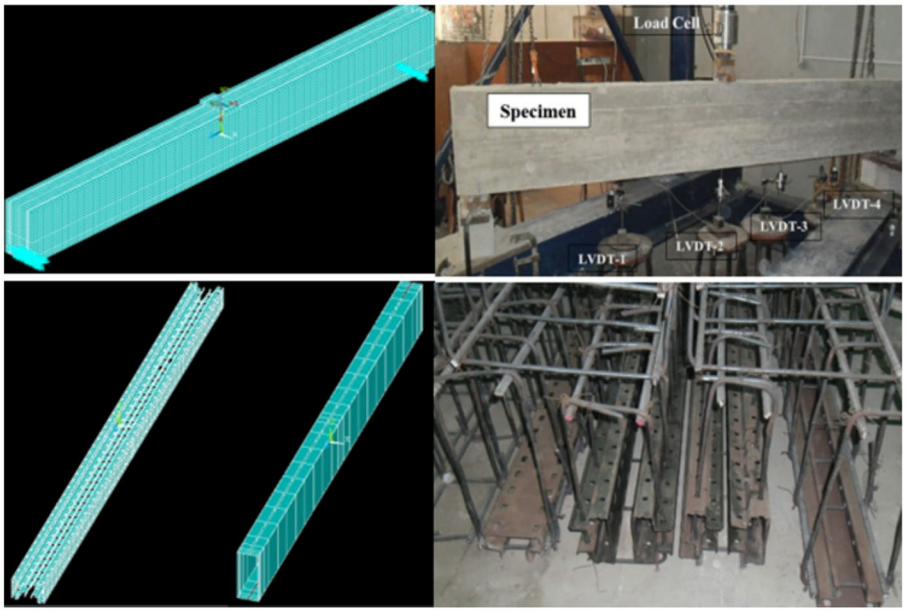

Fig. 1 Finite Elements simulation and meshing

strength (f_t) of 3.3 MPa, and a Poisson's ratio of 0.2. The nonlinear behavior of concrete was simulated using the SOLID65 element in ANSYS, incorporating the Willam–Warnke [20] failure criterion to capture cracking and crushing through a smeared-crack approach. Shear transfer coefficients were set to 0.2 for open cracks and 0.9 for closed cracks, following recommendations from previous validation studies [8]. Both the steel reinforcement and cold-formed steel (CFS) sections were simulated using a bilinear isotropic hardening model. For the reinforcing steel, a modulus of elasticity (E = 200 GPa) and a yield strength (f_y = 420 MPa) were used. The CFS sections were assigned a higher yield strength (f_y= 550 MPa) with a tangent modulus equal to 0.5% of E to accurately capture the post-yield behavior and strain hardening effects, consistent with typical high-strength cold-formed steel properties.

2.4 Boundary conditions and loading scheme

The modeled beams had concrete cross-sectional dimensions of 200 mm width and 400 mm depth, with an overall length of 3050 mm and a clear span of 2950 mm. To ensure numerical stability and reproducibility, the beams were modeled under simply supported conditions. Figure 2 illustrates a schematic explicitly illustrating these conditions and the incremental mid-span point-load arrangement. To prevent localized numerical singularities and premature failure at the contact zones, steel bearing plates were employed at both the support and the loading point. This configuration allowed for the precise tracking of crack propagation, strain development, and stiffness degradation throughout the automatic incremental load steps until ultimate failure.

3 Verification of finite element models

3.1 Experimental benchmark

Table 1 presents the experimental specimens from Abou-Rayan et al. [1] used for model validation. The verified models exhibited strong agreement in ultimate capacity, mid-span deflection, and failure modes. The experimental program was conducted to provide a baseline for FE validation. The composite beam specimens were tested using a hydraulic jack with a maximum capacity of 500 kN, integrated into a rigid steel testing frame. Mid-span deflections were measured using high-precision Linear Variable Differential Transformers (LVDTs) with a sensitivity of 0.01 mm, while the applied load was monitored through a calibrated load cell. The samples were prepared by accurately positioning the CFS sections within the formwork using specialized plastic spacers to maintain the design concrete cover of 25 mm, ensuring the geometric consistency required for reliable comparison with the numerical models.

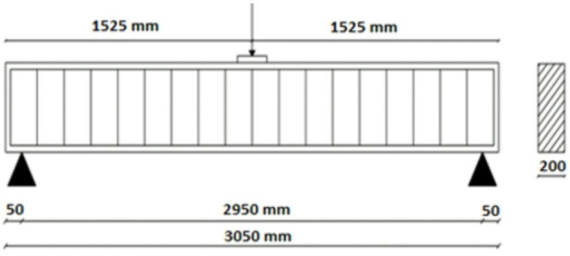

Fig. 2 Models boundary conditions

Table 1 Experimental specimens (Steel Section)

Specimen	Depth (mm)	Flange Width (mm)	Thickness (mm)	Section Position
A0	–	–	–	–
BFF1	305	62	1.5	Back-to-back
BFF2	305	62	1.5	Face-to-face
BFH1	305	31	1.5	Back-to-back
CTF1	120	62	2.4	Back-to-back
CTF2	120	62	2.4	Face-to-face
CTH1	120	31	2.4	Back-to-back
DSTF1	120	73.5	2.0	Back-to-back
DSTF2	120	73.5	2.0	Face-to-face
ESFH1	120	73.5	2.0	Horizontal
ESFH2	120	73.5	2.0	Horizontal inverted

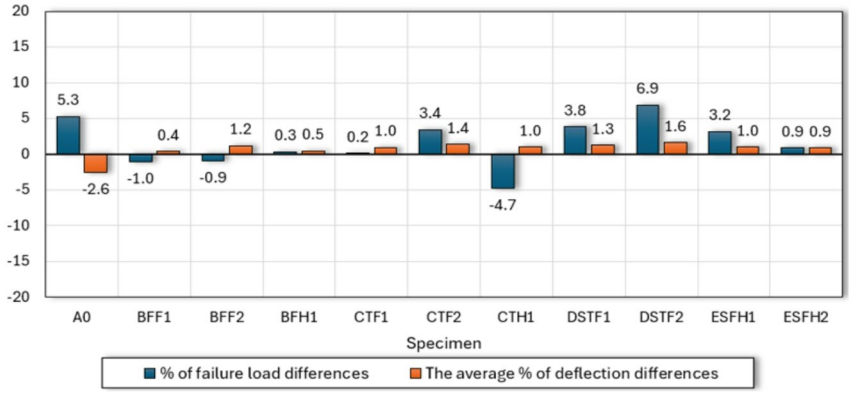

Fig. 3 Comparison of experimental and FE Load-deflection and Failure load results

3.2 Validation of the finite element model

The comparison between the experimental results and the Finite Element (FE) analysis demonstrated high accuracy, confirming the robustness and reliability of the developed numerical model. Figure 3 illustrates a detailed comparison of the experimental and numerical results in terms of the load–deflection behavior and ultimate load capacity of the tested specimens. Overall, the FE models successfully simulated the experimental response with high fidelity, effectively capturing the initial stiffness, the yielding point, and the post-peak softening stage. This strong correlation validates the adopted constitutive laws, boundary conditions, and meshing strategy used in the analysis. A rigorous error analysis was conducted to evaluate the predictive accuracy of the developed FE models against the experimental benchmarks. The discrepancies in the ultimate load capacities predicted by the FE models compared to the corresponding experimental values ranged only between − 4.7% and + 6.9%. Simultaneously, the average difference in mid-span deflection ranged between − 2.55% and + 1.63%. These minimal deviations fall well within the acceptable tolerance limits for numerical validation studies of composite beams. Although the FE results showed a slightly higher prediction of the ultimate load capacity compared to the experimental findings, which may be attributed to the idealization of loading and support conditions and the assumption of perfect bond in the numerical model, these discrepancies remain very limited. This methodical agreement proves that the proposed Finite Element model is an accurate and reliable tool for capturing the elastic and nonlinear behaviors of composite members encased with CFS

sections, thus establishing a sound basis for conducting comprehensive parametric studies and design optimization.

This methodical agreement proves that the proposed Finite Element model is an accurate and reliable tool for capturing the elastic and nonlinear behaviors of composite members encased with CFS sections, thus establishing a sound basis for conducting comprehensive parametric studies and design optimization. Analysis of the shear stress distribution within the composite section confirms that the encased CFS profiles provide substantial shear resistance. This contribution effectively mitigates the risk of premature diagonal tension failure (shear failure), ensuring that the composite members reach their predicted ultimate flexural capacity. The interaction between the steel webs and the concrete encasement creates a robust internal mechanism that enhances the overall structural integrity under concentrated loading.

3.3 Comparison of failure modes

A detailed comparison between the experimentally observed and numerically predicted failure modes was conducted to further validate the developed finite element (FE) model. The FE simulations successfully reproduced the same crack propagation pattern and overall failure shape observed in the laboratory tests. Specifically, a comparative analysis of failure mechanisms reveals that thinner CFS sections ($t < 1.5$ mm) tend toward more pronounced and premature local web buckling compared to thicker profiles. In contrast, perforated sections demonstrate a distinct transition from brittle concrete crushing to a more ductile response. This behavior is attributed to the 'plugging effect,' where the concrete plugs within the openings provide continuous lateral restraint to the steel webs, effectively delaying the onset of local instability and enhancing energy dissipation. Both the experimental and numerical specimens exhibited similar crack initiation at the support region, followed by flexural cracking in the tension zone and local buckling in the cold-formed steel (CFS) web. The agreement between experimental and FE crack patterns confirms that the adopted constitutive models for concrete cracking (SOLID65) and steel yielding (LINK180, SOLID185) captured material nonlinearity effectively. The predicted crushing zones and tension cracks were nearly identical in location and extent to those recorded in the experimental program. Overall, the close resemblance between the observed and simulated failure mechanisms verifies the reliability of the numerical model in reproducing both the global and local behavior of encased CFS beams under flexural loading.

4 Results and discussion

4.1 Experimental benchmark

A comprehensive parametric investigation was performed to evaluate the influence of key geometric and configuration parameters of cold-formed steel (CFS) sections on the flexural performance of concrete-encased composite beams. The validated finite element (FE) model was utilized to systematically vary three primary parameters: (i) CFS thickness, (ii) CFS section height, and (iii) CFS section configuration. Each parameter was analyzed for both smooth and perforated CFS sections to assess the effect of perforations on the structural response.

The first parameter examined was the CFS section thickness, varied from 1.0 to 4.0 mm while maintaining a constant section height of 360 mm (0.9 H). The second

Table 2 Parametric study Specimens

Number of Specimens	t (mm)	H (mm)	CFS arrangement				Variable
2	1	360	B - B F - F		F - F		Cold-formed steel section thickness
2	1.5	360	B - B F - F		F - F		
2	2	360	B - B F - F		F - F		
2	2.5	360	B - B F - F		F - F		
2	3	360	B - B F - F		F - F		
2	4	360	B - B F - F		F - F		
2	4	360	B - B F - F		F - F		CFS Height
2	4	300	B - B F - F		F - F		
2	4	200	B - B F - F		F - F		
2	4	100	B - B F - F		F - F		
4	4	200	B - B	F - F	U-Shape	n-Shape	CFS arrangement

*Each group repeated for Smooth and Perforated CFS in addition to Control Specimen. Total Specimens= 49 Specimens

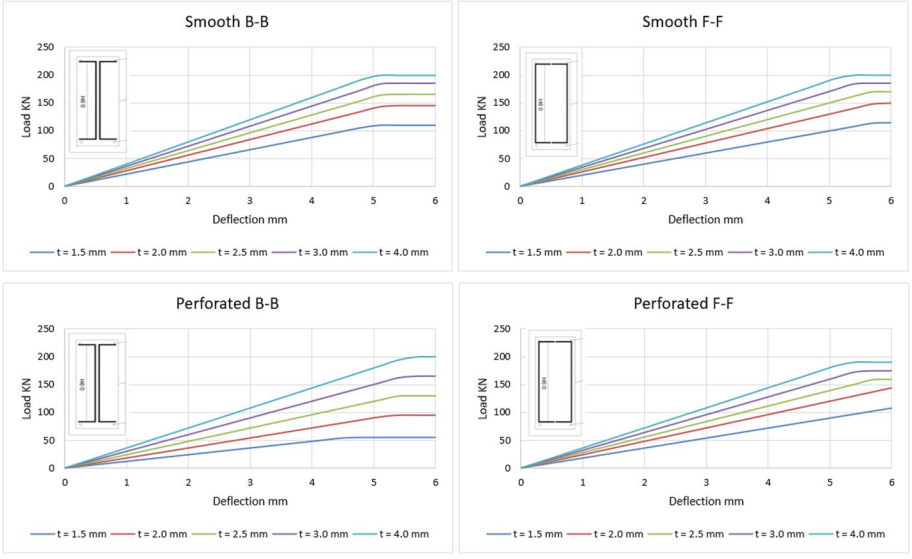

Fig. 4 Influence of CFS Thickness on Load-deflection relationships (constant height M = 0.9 and fixed perforation geometry per [1]

parameter was the section height, adjusted to 0.25 H, 0.5 H, 0.75 H, and 0.9 H of the concrete beam depth. Finally, the third parameter involved the CFS arrangement within the concrete section namely back-to-back (B–B), front-to-front (F–F), U-shape, and n-shape configurations. All analyses were conducted twice for smooth and perforated CFS specimens. The parametric matrix is summarized in Table 2.

The load-deflection relationships presented in Figs. 4 , 5, and 6 are presented to encompass the full structural response of the composite specimens. These curves clearly illustrate the initial linear elastic phase, followed by the initiation of material yielding

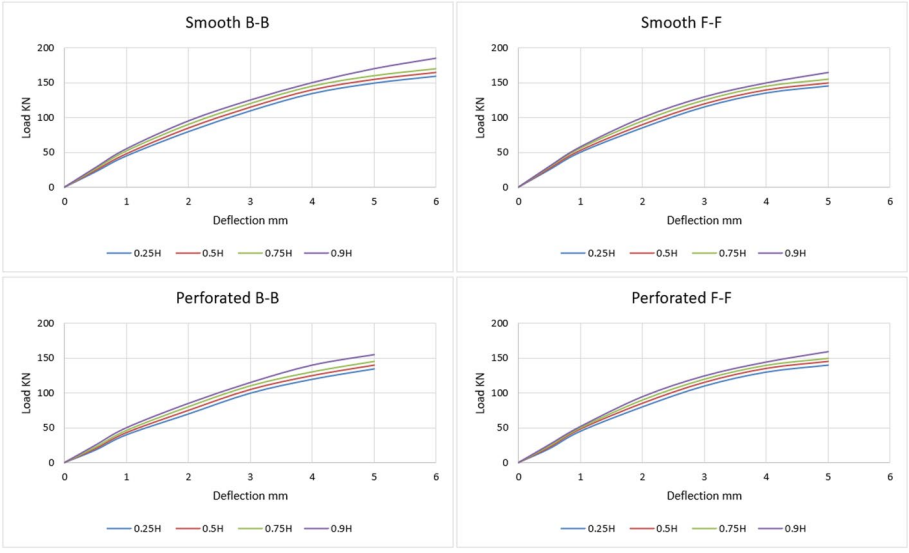

Fig. 5 Influence of CFS height on Load-deflection relationships (constant thickness t = 4 mm and fixed perforation geometry per [1]])

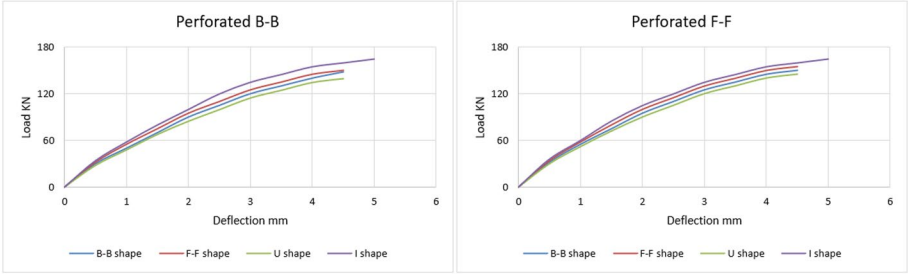

Fig. 6 Influence of CFS Configuration Type on Load-deflection relationships (constant thickness t = 4 mm, height H = 0.5 H, and fixed perforation geometry per [1])

and the subsequent post-peak softening stage until ultimate failure. By capturing the complete stress state, the numerical models provide a detailed assessment of the ductility and energy dissipation capacity of both smooth and perforated CFS-encased beams. This comprehensive representation confirms the model's ability to simulate complex failure mechanisms, including concrete crushing and the progression of local buckling in the steel webs.

4.2 Effect of CFS section thickness

Figure 4 presents the load–deflection relationships for different CFS thicknesses under both smooth and perforated configurations. Increasing the CFS wall thickness produced a substantial enhancement in both stiffness and ultimate capacity. For smooth B–B specimens, the ultimate load increased by 43% to 150% as the thickness rose from 1 mm to 4 mm compared with the control specimen. Similarly, smooth F–F specimens exhibited load gains of 63% to 120% within the same thickness range. When perforated sections were used, the improvement remained significant despite the presence of openings. Perforated B–B sections achieved capacity gains of 43–160%, while F–F sections exhibited increases of 56–118% relative to the control beam. Regarding the mechanistic insight, the FE analysis confirms that the reduced efficiency in perforated sections

is primarily due to the reduction in the net cross-sectional area of the steel web, which leads to localized stress concentrations around the opening perimeters. These concentrations accelerate the onset of local yielding on the web. However, this is partially offset by the 'plugging effect' of the concrete encased within the perforations, which provides lateral restraint against the thin-walled steel plates, thereby delaying local buckling and improving ductility. These findings indicate that increasing CFS thickness is the most influential parameter in enhancing the flexural resistance of the encased beams, with perforations only slightly reducing efficiency due to localized stress concentrations. This improvement can be attributed to delayed local buckling and enhanced composite interaction resulting from increased plate stiffness.

The parametric results indicate that the thickness ratio (K) has a more dominant role in governing the local stability of the thin-walled CFS components. Increasing thickness directly enhances the plate's slenderness ratio, thereby delaying the onset of local and distortional buckling modes. Mechanistically, a thicker CFS section provides a more rigid core that improves the overall confinement effectiveness of the concrete encasement, leading to a superior post-peak response and a more pronounced gain in ultimate load (Z). This is particularly evident in the B-B configuration, where the increased thickness works in tandem with the concrete 'plug' to prevent inward buckling of the webs.

4.3 Effect of CFS section height

Figure 5 illustrates the response of beams incorporating varying CFS heights with CFS thicknesses of 4 mm. For smooth B–B configurations, increasing the section height from 0.25 H to 0.9 H resulted in capacity gains ranging from 67% to 150% relative to the control beam, while the F–F arrangement achieved gains between 87% and 120%. In the case of perforated specimens, the B–B arrangement exhibited increases from 67% to 147%, and the F–F configuration showed gains from 82% to 118%. The results clearly indicate that deeper CFS sections enhance the flexural stiffness and delay crack initiation, as a larger steel depth improves moment resistance and composite interaction with the concrete matrix. It was observed that while increasing the CFS height significantly enhances the flexural capacity, the strength gain becomes marginal as the height ratio exceeds 0.9 H. Physically, this behavior occurs because the CFS flanges approach the extreme compression and tension fibers of the concrete section. At this stage, the concrete cover becomes insufficient to provide the necessary confinement and bond strength, leading to premature localized instability or concrete spalling as indicated by the FE stress distribution patterns. Therefore, a height ratio of 0.9 H is identified as the optimal threshold for maximizing composite action without compromising the protective role of the concrete cover.

Conversely, the height ratio (M) primarily influences the global flexural stiffness and the moment arm of the composite section. While increasing M raises the moment of inertia and consequently the ultimate capacity, its effect is bounded by the concrete cover integrity. At high M values (above 0.9), the reduced concrete cover leads to premature spalling and a loss of bond between the steel and concrete, which explains the plateau in strength gain observed in Figs. 8 and 9. Therefore, while height provides global strength, thickness is the key parameter for ensuring the local stability and ductility required for efficient composite action.

4.4 Effect of CFS section configuration

The influence of the CFS configuration was evaluated for both smooth and perforated sections with constant thickness (t = 4 mm) and height (H = 0.5 H). As shown in Fig. 6, the smooth B–B, F–F, U, and n-shaped sections improved ultimate loads by 91%, 93%, 91%, and 72%, respectively, compared to the control specimen. For perforated sections, the corresponding improvements were 87%, 82%, 97%, and 53%. Among all configurations, the front-to-front and U-shaped arrangements demonstrated superior load-carrying efficiency due to enhanced confinement of the concrete core and improved stress distribution along the beam depth. The n-shape arrangement exhibited relatively lower strength due to weaker composite interaction and reduced section symmetry.

Overall, the parametric results reveal that increasing CFS thickness provides the most significant improvement in beam capacity and stiffness. Increasing CFS height enhances the flexural strength up to 0.9 H, beyond which gains become marginal. The front-to-front and U-shaped configurations outperform other arrangements, while perforations slightly reduce strength but improve ductility by delaying concrete spalling. The FE-predicted load–deflection responses show consistent stiffness trends across all parameters, confirming the model's ability to capture nonlinear behavior accurately.

A direct comparison between smooth and perforated CFS-encased beams reveals distinct trade-offs in structural performance. While smooth sections generally exhibit higher ultimate strength and initial stiffness due to the intact net cross-sectional area of the steel web, perforated sections demonstrate superior post-peak behavior and energy dissipation, quantified by a higher Ductility Index. For the B-B configuration, the ultimate load gain Z for perforated specimens reached 160%, surpassing the 150% achieved by smooth specimens at K = 4, which underscores the significant contribution of mechanical interlocking. This variation is primarily attributed to the 'plugging effect' of the concrete. Although the perforations reduce the net steel area and introduce localized stress concentrations, the concrete plugs within these openings provide continuous lateral restraint to the thin-walled steel plates. This mechanistic interaction effectively delays the onset of local buckling and transforms the failure mode into a more ductile response. Consequently, while the smooth sections provide a reliable baseline for global strength, the perforated configurations offer a more resilient solution for applications requiring enhanced ductility and robust composite interaction.

4.5 Empirical formulas for flexural strength prediction

To generalize the FE findings for design use, a systematic regression analysis was performed on the parametric dataset consisting of 49 validated models. The derivation process involved evaluating various functional forms, where high-order polynomial regression (third and fourth degree) was identified as the most robust approach to ensure the maximum possible accuracy. Physically, the necessity for these high-order models arises from the highly nonlinear stress redistribution that occurs as the CFS flanges approach the extreme compression and tension fibers of the concrete section. While simplified linear or quadratic models fail to capture the complex 'plateau' effect observed at height ratios M > 0.9 where concrete cover integrity becomes a limiting factor, the proposed high-order equations precisely model this transition. Consequently, these models achieved a coefficient of determination ($R^2 > 0.98$), proving their superior

predictive accuracy for the complex composite interactions between the steel sections and surrounding concrete. Figure 7 presents the developed empirical equations predicting the enhancement in ultimate flexural capacity (Z). In these models, the physical parameters are defined as follows: (Z) represents the ultimate load gain ratio, (K) is the normalized thickness ratio ($t_{CFS}/b_{concrete}$%), and (M) is the relative height ratio ($H_{CFS}/H_{Concrete}$%). The formulas express the relationship between these geometric ratios and the ultimate load gain.

The polynomial trendlines exhibit excellent agreement with the finite element results ($R^2 > 0.98$), accurately capturing the nonlinear interaction between the encased steel and surrounding concrete. The derived models confirm that increasing either K or M significantly enhances the flexural resistance, particularly for perforated sections where interfacial bonding improves stress transfer. It should be noted that the applicability of these formulas is limited to the parametric range studied, specifically for thickness ratios (K) between 1.0% and 4.0% and height ratios (M) between 0.25 and 0.9.

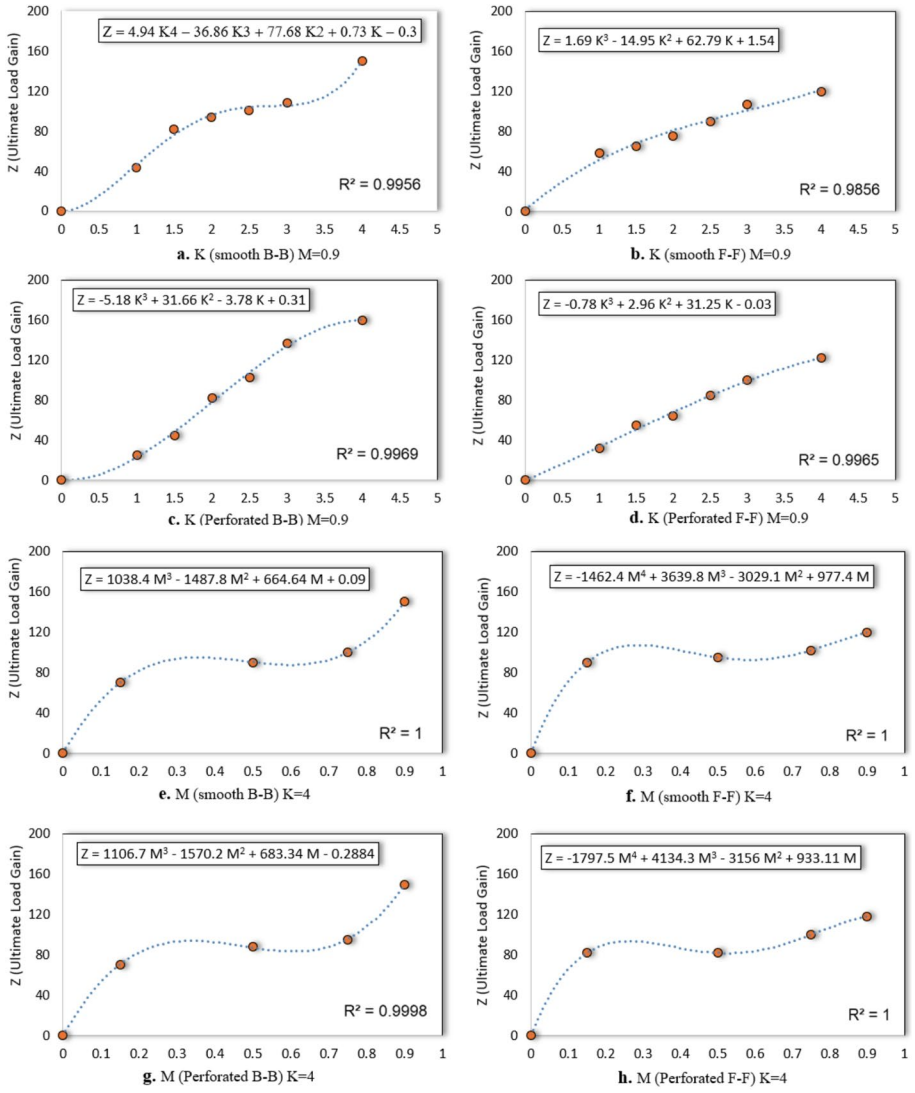

Fig. 7 Predicted relationships between Ultimate Load Gain (Z) and geometric ratios (K and M) for smooth perforated CFS-encased beams

These equations offer a practical tool for optimization and parametric design, enabling rapid estimation of ultimate capacity without the need for time-consuming FE analyses. Their integration into design optimization frameworks can support efficient geometry selection, balancing strength, material use, and cost effectiveness. The derived equations can serve as a foundation for multi-objective optimization algorithms aiming to minimize material use while maximizing structural efficiency.

To provide a robust design framework, a set of empirical equations was derived through high-order polynomial regression analysis of the parametric FE database, as summarized in Table 3. These equations characterize the ultimate load gain (Z as a function of the thickness ratio (K) and height ratio (M) for both Back-to-Back (B-B) and Front-to-Front (F-F) arrangements. For the B-B configuration, the equations accurately capture the nonlinear enhancement provided by the 'plugging effect' in perforated sections, which leads to a maximum gain of 160%. Similarly, the equations for the F-F configuration account for the inherent confinement provided by the closed-loop geometry, where smooth sections maintain high efficiency across mid-range height ratios. The high order of these polynomials (up to the 4th degree) ensures that the complex interaction between the steel profiles and the surrounding concrete is precisely modeled, offering a reliable alternative to computationally expensive FE simulations for preliminary structural design.

The unified design chart presented in Fig. 8 offers a practical tool for the structural optimization of the Back-to-Back (B-B) configuration. By mapping the ultimate load gain (Z) against both thickness (K) and height (M) ratios, the chart highlights the superior performance of perforated sections at higher thickness ratios. Specifically, for $K > 2.5$, perforated B-B sections achieve up to 160% strength enhancement, surpassing smooth sections by approximately 10% due to the increased mechanical interlocking (plugging effect) provided by the web openings. Conversely, both configurations exhibit consistent convergence at a height ratio of $M = 0.9$, which is identified as the optimal threshold for maximum flexural capacity. To ensure the reliability of the proposed equations (Z-K and Z-M), it is essential to note that their validity is constrained to the geometric and material ranges investigated in this study. Specifically, these models are applicable for thickness ratios (K) between 0% and 4.0% and height ratios (M) from 0 to 0.9. Application beyond these limits, particularly for very thin concrete covers ($M > 0.95$), may lead to inaccuracies due to the increased risk of concrete spalling and loss of composite integrity.

Similarly, the comparative performance for the Front-to-Front (F-F) arrangement is illustrated in Fig. 9. Like the B-B configuration, the F-F arrangement shows a consistent increase in load gain (Z) with the enhancement of K and M ratios. For smooth F-F

Table 3 Proposed empirical design equations for predicting the ultimate load gain

K	M	CFS arrangement	Z	R^2
Variable	0.9	smooth B-B	$4.94\,K^4 - 36.86\,K^3 + 77.68\,K^2 + 0.73\,K - 0.3$	0.996
Variable	0.9	smooth F-F	$1.69\,K^3 - 14.95\,K^2 + 62.79\,K + 1.54$	0.986
Variable	0.9	Perforated B-B	$-5.18\,K^3 + 31.66\,K^2 - 3.78\,K + 0.31$	0.997
Variable	0.9	Perforated F-F	$-0.78\,K^3 + 2.96\,K^2 + 31.25\,K - 0.03$	0.997
4	Variable	smooth B-B	$1038.4\,M^3 - 1487.8\,M^2 + 664.64\,M + 0.09$	1
4	Variable	smooth F-F	$-1462.4\,M^4 + 3639.8\,M^3 - 3029.1\,M^2 + 977.4\,M$	1
4	Variable	Perforated B-B	$1106.7\,M^3 - 1570.2\,M^2 + 683.34\,M - 0.2884$	1
4	Variable	Perforated F-F	$-1797.5\,M^4 + 4134.3\,M^3 - 3156\,M^2 + 933.11\,M$	1

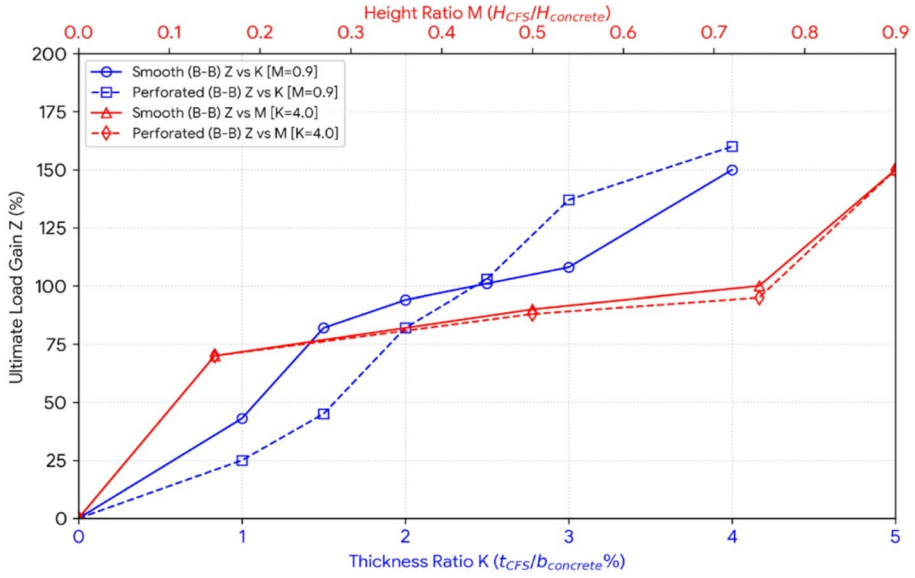

Fig. 8 Combined Design Chart for estimating ultimate load gain (Z) for Back-to-Back (B-B) smooth and perforated CFS-encased beams

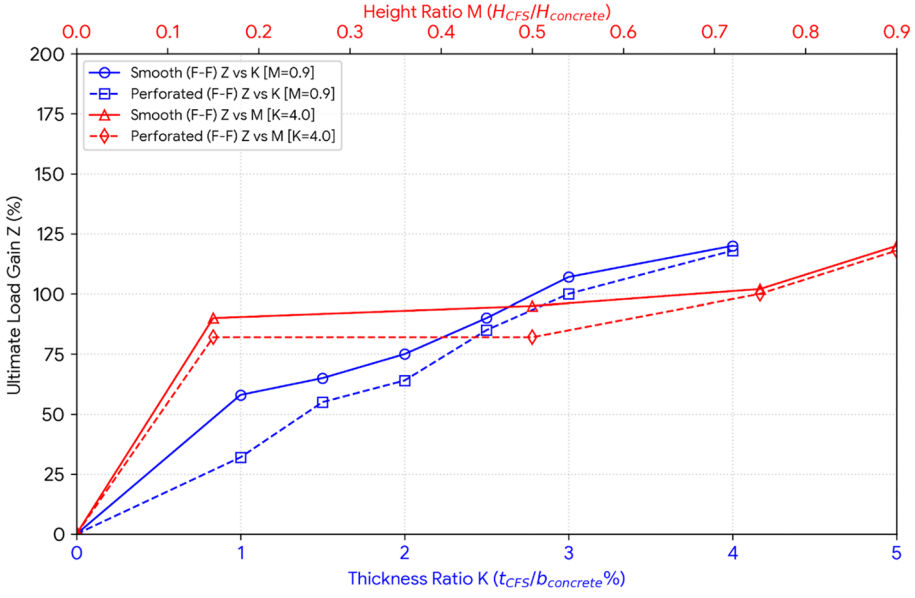

Fig. 9 Combined Design Chart for estimating ultimate load gain (Z) for Front-to-Front (F-F) smooth and perforated CFS-encased beams

sections, the ultimate load gain reaches 120% at K = 4, whereas the perforated F-F sections achieve a comparable gain of 118%. A key observation is the stability of strength gain across intermediate height ratios; for instance, at M = 0.5, the smooth F-F section maintains a gain of 95%, slightly higher than the 82% observed for the perforated variant. This suggests that while perforations facilitate mechanical interlock, the closed-loop nature of the F-F geometry provides inherent confinement that makes the smooth web slightly more efficient at mid-range depths.

5 Conclusions

This research presented an integrated numerical investigation into the flexural performance of RC beams encased with smooth and perforated CFS sections. Based on the validated FE results and the extensive parametric study, the following novel findings are concluded:

- The developed 3-D nonlinear FE model accurately predicts flexural behavior, with a minimal discrepancy of ±7% in ultimate capacity compared to experimental benchmarks.
- Increasing CFS thickness (K) and height (M) are the most critical factors for enhancing stiffness and ultimate load; however, thickness is the primary parameter governing the local stability of the thin-walled CFS plates.
- The study uniquely quantifies the 'plugging effect' within CFS perforations. This mechanical interlock provides continuous lateral restraint to the steel webs, effectively delaying local buckling and transforming failure modes into more ductile responses.
- The front-to-front (F-F) and U-shaped configurations provide superior load-carrying efficiency compared to the n-shaped layout due to the improved confinement of the concrete core.
- A novel set of high-order empirical formulas and unified design charts ($R2 > 0.97$) identify an optimal design configuration at $M = 0.9$ and $K >= 2.5\%$. In this range, the enhanced composite interaction allows perforated configurations to achieve a peak load gain of 160%, surpassing smooth Sect. (150%) by leveraging the synergy between global stiffness and the mechanical 'plugging effect'.
- From a practical perspective, F-F and U-shaped configurations are recommended for modular construction due to their superior confinement. Furthermore, web perforations are strategically encouraged for seismic-prone regions to enhance energy dissipation, provided the identified optimal matching range is maintained.

6 Future Work

To further advance the understanding of composite CFS-encased members, the following directions are proposed:

- Extending the current numerical framework to evaluate the structural performance under cyclic and seismic loading conditions to assess energy dissipation capacity.
- Investigating the behavior of encased perforated sections under fatigue and long-term environmental effects.
- Exploring the use of innovative infill materials, such as recycled aggregate concrete or high-performance fiber-reinforced composites, to further optimize the strength-to-weight ratio.
- Investigating the influence of varied perforation geometric parameters, such as opening shapes (circular, rectangular, or elliptical), staggered arrangements, and opening ratios, to broaden the universality of the proposed design models.

Author contributions

M.E. and N.K. conceived and designed the finite element models. M.E. performed the numerical simulations and data collection. A.A. and A.Y.K. validated the numerical results against experimental benchmarks. M.E. and N.K. developed the empirical design formulas and performed the parametric analysis. M.E., N.K., and A.A. wrote the main manuscript text. A.Y.K. and A.A. prepared the figures and tables. All authors reviewed and edited the manuscript.

Funding
This research did not receive any specific grant from funding agencies in the public, commercial, or non-profit sectors.

Data availability
The data sets generated during and/or analyzed during the current study are available from the corresponding author on reasonable request.

Declarations

Ethics approval and consent to participate
Not applicable.

Competing interests
The authors declare no competing interests.

Clinical trial number
Not applicable.

Received: 20 December 2025 / Accepted: 9 April 2026
Published online: 24 April 2026

References

1. Abou-Rayan A, Khalil N, Youssef AK, Eldeib M. Flexural behavior of encased beam flat or perforated steel cold-formed sections. Int J Steel Struct. 2021;21:1465–77. https://doi.org/10.1007/s13296-021-00515-9.
2. Al Zand AW, Alghaaeb MF, Liejy MC, Mutalib AA, Al-Ameri R. Stiffening performance of cold-formed C-section beam filled with lightweight-recycled concrete mixture. Materials. 2022;15(9):2982. https://doi.org/10.3390/ma15092982.
3. Chandramohan DL, Roy K, Beulah Gnana Ananthi G, Fang Z, Lim JB. Structural behaviour and capacity of cold-formed steel channel sections with elongated edge-stiffened and unstiffened web holes under compression. J Constr Steel Res. 2024;218:108681. https://doi.org/10.1016/j.jcsr.2024.108681.
4. Chandramohan DL, Roy K, Fang Z, Ananthi. G BG, Lim JB. Moment capacity of cold-formed steel channel beams with edge-stiffened and unstiffened elongated web holes. Thin-Walled Struct 206(Part A). 2025;112605. https://doi.org/10.1016/j.tws.2024.112605.
5. Degtyareva N, Pologanathan K, Mahendran M. Web crippling tests of cold-formed steel channels with staggered web perforations. Thin-Walled Struct. 2021;159:107314. https://doi.org/10.1016/j.tws.2020.107314.
6. Dwivedi R, Vyavahare AY. Web crippling behavior of perforated cold-formed Z-sections under end-two-flange loading. Mater Today: Proc. 2022;65(2):615–21. https://doi.org/10.1016/j.matpr.2022.03.196.
7. Elkassas E, Morsy AM, Marzouck M. Flexure behavior of hollow steel beams strengthening with ferrocement. J Eng Appl Sci. 2022;69:86. https://doi.org/10.1186/s44147-022-00123-2.
8. Haidarali MR, Nethercot DA. Finite element modelling of cold-formed steel beams under local buckling or combined local/distortional buckling. Thin-Walled Struct. 2011;49(12):1554–62. https://doi.org/10.1016/j.tws.2011.08.003.
9. Liejy MC, Al Zand AW, Mutalib AA, Sulong NHR. Flexural performance of a novel steel cold-formed beam–PSSDB slab composite system filled with concrete material. Buildings. 2023;13(2):432. https://doi.org/10.3390/buildings13020432.
10. Lotfy O, Gaawan S, Yehia M. Experimental investigation of the behaviour of perforated steel cold-formed column encased in lightweight concrete. Eng Res J. 2024;183(3):165–90. https://doi.org/10.21608/erj.2024.377299.
11. Ma W, Becque J, Hajirasouliha I, Ye J. Cross-sectional optimization of cold-formed steel channels to Eurocode 3. Eng Struct. 2015;101:641–51. https://doi.org/10.1016/j.engstruct.2015.07.051.
12. Nawar MT, Silem OA, Ibrahim I, Maaly HM, Ibrahim YE. Enhancing the toughness of composite cold-formed steel beams with ECC and different stiffener arrangements and shapes. J Compos Sci. 2025;9(1):24. https://doi.org/10.3390/jcs9010024.
13. Pham NH, Tusnin A, Vatin N, Doroshenko A. Flexural capacities of cold-formed steel channel sections with perforations. Lect Notes Civ Eng. 2023;282:179–87. https://doi.org/10.1007/978-3-031-10853-2_17.
14. Pologanathan K, Mahendran M. Experimental investigation and design of lipped channel beams in shear. Thin-Walled Struct. 2015;86:174–84. https://doi.org/10.1016/j.tws.2014.08.024.
15. Serror MH, Hassan EM, Mourad SA. Experimental study on the rotation capacity of cold-formed steel beams. J Constr Steel Res. 2016;121:216–28. https://doi.org/10.1016/j.jcsr.2016.02.005.
16. Shen J, Zhang X, Wu P, Yue K, Chen J. Experimental and finite element analysis of bending performance of web-embedded double inverted T-shaped steel–concrete composite beams. Buildings. 2025;15(5):717. https://doi.org/10.3390/buildings15050717.
17. Sheta A, Ma X, Zhuge Y, ElGawady MA, Mills JE, Abd-Elaal E. Flexural strength of innovative thin-walled composite cold-formed steel/PE-ECC beams. Eng Struct. 2022;267:114675. https://doi.org/10.1016/j.engstruct.2022.114675.
18. Vadivelu C, Prabaharan V, Akhas PK. Flexural behavior of perforated rectangular hollow section cold-formed steel beams: an experimental and numerical study. Results Eng. 2025;26:104821. https://doi.org/10.1016/j.rineng.2025.104821.
19. Wang L, Miller R. Advanced numerical modeling of thin-walled steel sections encased in ultra-high-performance concrete. Eng Struct. 2026;335:120540. https://doi.org/10.1016/j.engstruct.2025.120540.
20. Willam KJ, Warnke EP. Constitutive model for the triaxial behavior of concrete. Proc IABSE. 1975;19(1):1–30.
21. Yao B, Shi Y, Wang W, Zhang L. Flexural behavior of cold-formed steel composite floor infilled with desert sand foamed concrete. Buildings. 2023;13(5):1217. https://doi.org/10.3390/buildings13051217.
22. Youssef AK, Khalil N. Composite concrete beam with multi-web cold-formed steel section. Chall J Concrete Res Lett. 2019;10(2):20–33. https://doi.org/10.20528/cjcrl.2019.02.001.
23. Youssef AY, Khalil N. Cold-Formed Steel U-Section Encased in Simple Support Reinforced Concrete Beam. J Mech Civil Eng (IJRDO). 2017;3(10):1–16. ISSN: 2456 – 1479.

24. Yu S, Yang K, Guan Y, Yao X, Xu L, Zhang H. The flexural behavior of cold-formed steel composite beams. Eng Struct. 2020;218:110819. https://doi.org/10.1016/j.engstruct.2020.110819.

Publisher's note